Sensors and Actuators B 147 (2010) 554–560

Contents lists available at ScienceDirect

Sensors and Actuators B: Chemical

journal homepage: www.elsevier.com/locate/snb

Synthesis and gas-sensing properties of nano- and meso-porous MoO_3-doped SnO_2

Azam Anaraki Firooz[a,b], Takeo Hyodo[a,*], Ali Reza Mahjoub[b], Abbas Ali Khodadadi[c], Yasuhiro Shimizu[a]

[a] Department of Materials Science and Engineering, Faculty of Engineering, Nagasaki University, 1-14 Bunkyo-machi, Nagasaki 852-8521, Japan
[b] Department of Chemistry, Tarbiat Modares University, 14115-175 Tehran, Iran
[c] School of Chemical Engineering, University of Tehran, 11155-4563 Tehran, Iran

ARTICLE INFO

Article history:
Received 16 December 2009
Received in revised form 6 March 2010
Accepted 8 March 2010
Available online 15 March 2010

Keywords:
SnO_2
Porous structure
MoO_3
Gas sensor
Ultrasonic spray-pyrolysis

ABSTRACT

Nano- and meso-porous SnO_2 powders doped with and without 1–10 wt% MoO_3 have been synthesized by an ultrasonic spray-pyrolysis method employing a precursor aqueous solution containing tin (IV) chloride pentahydrate ($SnCl_4{\cdot}5H_2O$), ammonium heptamolybdate and polymethylmethacrylate (PMMA) microspheres as a template, and the effects of MoO_3-doping and the addition of PMMA microspheres on the structural, morphological and gas-sensing properties of SnO_2 were investigated in this study. It is confirmed that control of the amounts of PMMA microspheres in the precursor solution was effective in realizing well-developed nano- and meso-porous structures of SnO_2 by X-ray diffraction analysis, scanning electron microscopy, transmission electron microscopy, X-ray photoelectron spectroscopy, and the measurement of specific surface area and pore size distribution using a N_2 adsorption isotherm. Gas-sensing properties of their thick films (about 50 μm thick), which were fabricated by screen-printing to various gases (NO_2, C_2H_5OH and H_2) were tested in ambient air. The doped thick films showed a high response and selectivity to 5 ppm NO_2 gas in the case of 10 wt% MoO_3-doping in both nano- and meso-porous structures of SnO_2. We observed that the presence of Mo species in SnO_2 lattice can improve the sensor response and selectivity towards NO_2 gas. The effect of the MoO_3-doping on the sensing characteristics of these films towards NO_2 was discussed.

1. Introduction

In recent years, much effort has been devoted to the synthesis of nanostructured tin oxide with specific morphology because of their novel optical, electrical and catalytic properties [1–3]. There are two ways that can improve these properties of SnO_2. One is doping of a metal or metal oxide into SnO_2 structure, which would induce a significant effect on its physical and chemical properties [4,5]. Another one is to synthesize nanostructured SnO_2, which would contribute to the achievement of a high specific surface area and quantum size effects [6,7]. The strict control of novel nano/microstructures with well-defined shape and doped with a metal or metal oxide may open new opportunities for exploring unique physical and chemical properties and more potential applications [8,9]. Therefore, development of morphologically controllable synthesis of SnO_2 nano/microstructures doped with a metal or metal oxide is urgently important to answer the demand for exploring the potentials of SnO_2 [10]. Nowadays, the addition of MoO_3 to SnO_2 has been devoted to obtain good morphological SnO_2/MoO_3 nanostructures in order to improve the sensing characteristics. MoO_3 is n-type semiconductor that can change the acidity performances of SnO_2 surfaces against reactivity with different gases [11,12]. The introduction of MoO_3 reduces the electrical conductivity of SnO_2 by two orders of magnitude in air, which may be due to the transfer of electrons trapped at oxygen vacancies to Mo^{6+} [13].

Generally, it is difficult to control the size and morphology of the oxide composites, which have important influence on their physical and chemical properties. In order to improve selectivity and sensor response to a particular target gas, we prepared a series of SnO_2 doped with and without MoO_3 (0–10 wt%) by ultrasonic spray-pyrolysis of the precursor mist and also performed a detailed analysis of the morphology and chemical states by scanning electron microscopy (SEM), transmission electron microscopy (TEM) and X-ray photoemission spectroscopy (XPS), to explain the changes in the sensing characteristics.

2. Experimental

In this paper, we synthesized two different structures, nano- and meso-porous SnO_2 doped with and without MoO_3 by ultrasonic spray-paralysis. $SnCl_4{\cdot}5H_2O$ and $(NH_4)_6Mo_7O_{24}$ were used as a raw

* Corresponding author. Tel.: +81 95 819 2645.
E-mail address: hyodo@nagasaki-u.ac.jp (T. Hyodo).

0925-4005/$ – see front matter © 2010 Elsevier B.V. All rights reserved.
doi:10.1016/j.snb.2010.03.021

material of a host (SnO_2) and a dopant, respectively, and a PMMA microsphere was added as a template in the precursor solution.

Porous SnO_2 doped with and without MoO_3 (1, 5, and 10 wt%) were synthesized via ultrasonic spray-pyrolysis (USP) with a specially designed mist-supply to prepare a porous SnO_2 powder in an electric furnace heated at 1100 °C [14]. 0.005 mol $SnCl_4{\cdot}5H_2O$ and $(NH_4)_6Mo_7O_{24}$ were dissolved in 50 mL H_2O separately. Mixing of these solutions was done using a magnetic stirrer for 3 h, followed by the addition of 3 or 5 g PMMA microspheres (Soken Chem. & Eng. Co., Ltd., 150 nm in diameter). The porous SnO_2 doped with and without MoO_3 obtained were denoted as pr-*m*MoO_3–SnO_2(*n*) or pr–SnO_2(*n*) (*n*: the amount of PMMA microspheres in the precursor solution (3 and 5 g), *m*: the amount of Mo addition (1, 5 and 10 wt%)), respectively. Using 3 and 5 g PMMA microspheres caused to get nano- and meso-porous structures, respectively, as will be confirmed later. The morphologies of pr–SnO_2(*n*) and pr-*m*MoO_3–SnO_2(*n*) powders were observed by SEM (JEOL Ltd., JSM-7500F) and TEM (JEOL Ltd., JEM2010-HT). The specific surface area and pore size distribution were measured by BET and BJH methods using a N_2 adsorption isotherm (Micromeritics, Tristar3000). Crystal phase and mesoporous structure of the samples were characterized by X-ray diffraction analysis (XRD; Rigaku Corp., RINT2200) using Cu Kα radiation (40 kV, 40 mA). The change in chemical states was measured with X-ray photoelectron spectroscopy (XPS, Kratos Analytical Ltd., AXIS-ULTRA DLD).

Thick film sensors (about 50 μm thick) were fabricated by screen-printing of pr–SnO_2(*n*) or pr-*m*MoO_3–SnO_2(*n*) powders on alumina substrates equipped with a pair of interdigitated Pt electrodes (the distance between Pt electrodes is ca. 200 μm), followed by calcination at 400 °C for 5 h. Gas responses of these sensors were measured to 5 ppm NO_2 balanced with air in a flow apparatus at 250–400 °C in order to find out the optimum operating temperature, and these sensors were stabilized for 5 h at the working temperature before exposure to the target gas. Sensor response was defined as the ratio (R_a/R_g) of sensor resistance in air (R_a) to that in gas balanced with air (R_g). To investigate the selectivity of the sensors to NO_2 gas, the responses to other reducing gases such as C_2H_5OH (100 ppm) and H_2 (1000 ppm) were also examined and compared with those to NO_2 gas.

3. Results and discussion

3.1. Characterization of pr–SnO_2(*n*) and pr-*m*MoO_3–SnO_2(*n*) powders

Fig. 1 shows the X-ray diffraction patterns of all samples. All the prominent peaks in the pattern corresponded to the rutile structure of SnO_2, which is indexed on the basis of JCPDS file No. 41-1445. No peaks corresponding to MoO_3 were observed; indicating that MoO_3 may incorporate into the tin oxide lattice. The full width at half maximum (FWHM) slightly changed with the addition of MoO_3. The data showed that FWHMs of pr-*m*MoO_3–SnO_2(*3*) and pr-*m*MoO_3–SnO_2(*5*) tended to increase and decrease with the additive amounts of MoO_3, respectively. Also, the variations in the lattice parameters were shown in Fig. 1. It is seen that on doping of MoO_3 in pr–SnO_2(*3*) and pr–SnO_2(*5*) a marginal decrease and increase in the '*a*' parameters is observed in all the concentrations, respectively, while '*c*' (*c* = 3.195 Å) remains almost unchanged in all samples. These parameters were in good agreement with crystallite size.

Fig. 2 shows SEM photographs of all samples. The microstructural morphology of all samples reflected the shape of submicron-size PMMA microspheres (*d*: 150 nm), but the diameter of the macropores was about 50–100 nm. It was smaller than the PMMA diameter, probably due to the slower pyrolysis rate of PMMA than that of tin chloride and shrinkage by the growth of SnO_2 crystallites [14]. In addition, the macropores of pr–SnO_2(*3*) and pr-*m*MoO_3–SnO_2(*3*) powders were hallow spheres, while those of pr–SnO_2(*5*) and pr-*m*MoO_3–SnO_2(*5*) powders were largely destroyed (the pores were not spheres). It seemed that the presence of many PMMA microspheres led to deformation of these pores. Fig. 3 shows schematically the formation mechanism of these samples. In case of pr-*m*MoO_3–SnO_2(*3*) powders, PMMA microspheres were relatively dispersed in the droplets of precursor solution, because the amount of PMMA microspheres was small. Therefore, the spherical pores reflecting the shape of PMMA microspheres remained uniformly and the oxide walls were formed stably among these pores, even after burning of PMMA and decomposition of the precursors, as shown in Fig. 2(a)–(d). In case of pr-*m*MoO_3–SnO_2(*5*) powders, on the other hand, the distances among the PMMA microspheres reduced by an increase of their numbers in the droplets, because the amount of oxide precursors was much less than that of PMMA microspheres in the droplets. Therefore, the oxide walls with mechanical stability could not be formed among the pores during the burning, and thus the obtained pores and oxide walls likely destroyed in the pr-*m*MoO_3–SnO_2(*5*) powders.

Figs. 4 and 5 show pore size distribution and specific surface area (SSA) of all samples. As shown in Fig. 4, the surface area and the amount of nanopores with a size of 2–4 nm in diameter of pr-*m*MoO_3–SnO_2(*3*) powders increased with an increase in the amount of MoO_3. In contrast, as shown in Fig. 5, the addition of 5 g PMMA microspheres in the precursor solution caused to decrease the surface area with an increase in the amount of

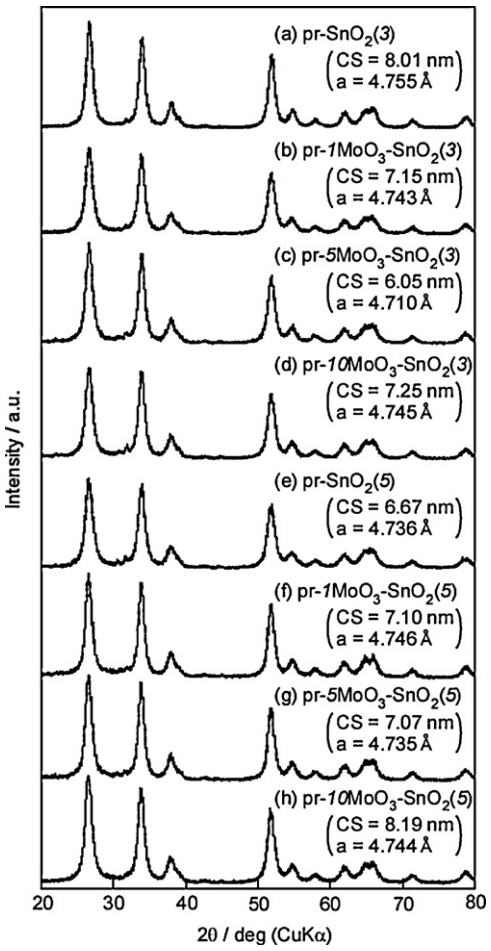

Fig. 1. XRD patterns of (a) pr–SnO_2(*3*), (b–d) pr-*m*MoO_3–SnO_2(*3*), (e) pr–SnO_2(*5*) and (f–h) pr-*m*MoO_3–SnO_2(*5*) powders (*m* = 1, 5 and 10), along with their crystallite size (CS) and lattice parameter (*a*).

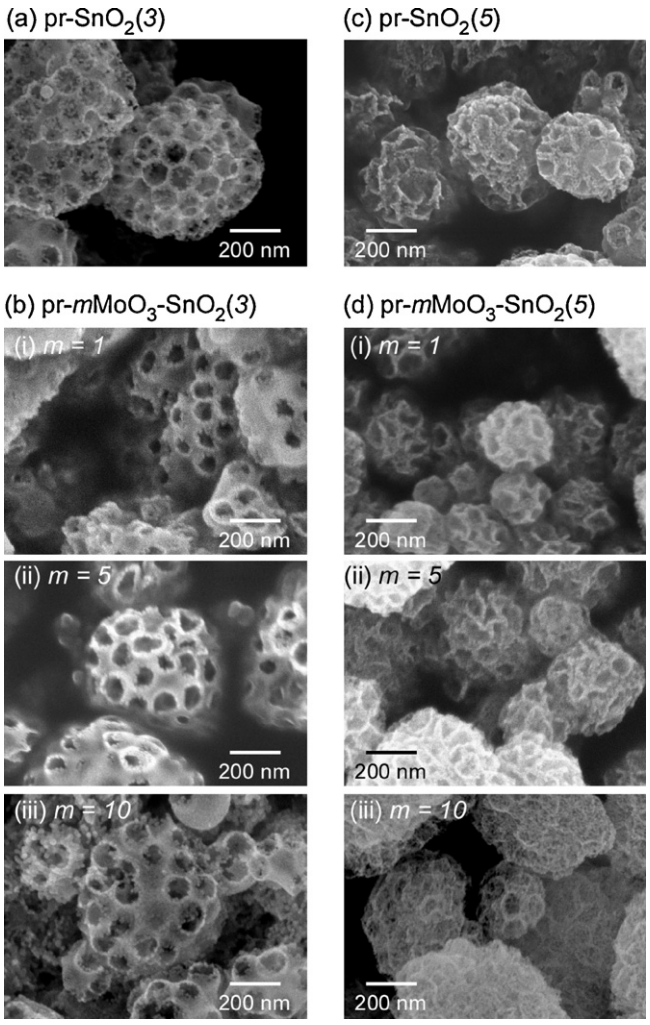

Fig. 2. SEM images of (a) pr–$SnO_2(3)$, (b) pr-$m$$MoO_3$–$SnO_2(3)$, (c) pr–$SnO_2(5)$ and (d) pr-$m$$MoO_3$–$SnO_2(5)$ powders.

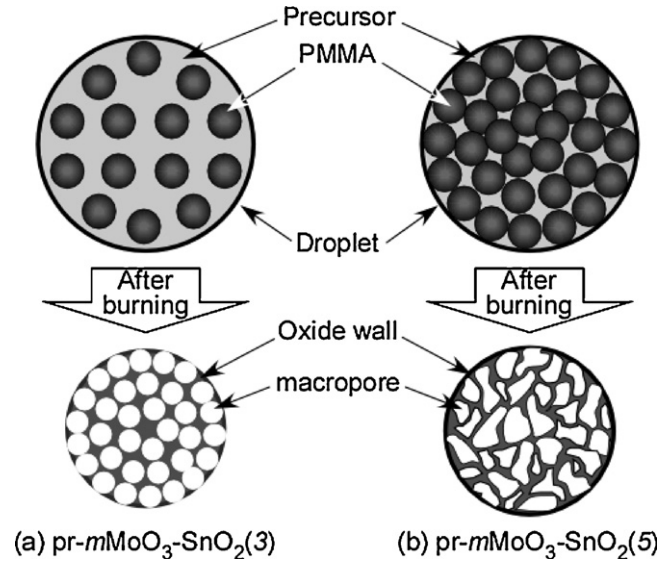

Fig. 3. Schematic drawing of formation mechanism of pores in (a) pr-$m$$MoO_3$–$SnO_2(3)$ and (b) pr-$m$$MoO_3$–$SnO_2(5)$.

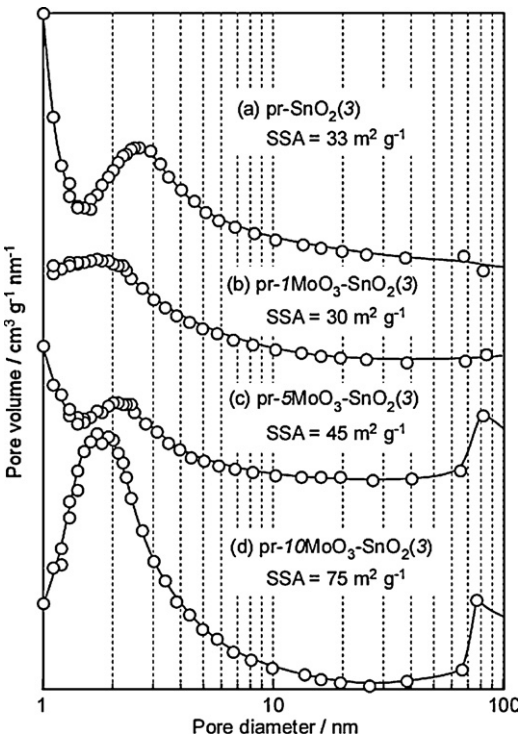

Fig. 4. Pore size distributions of pr–$SnO_2(3)$ and pr-$m$$MoO_3$–$SnO_2(3)$ powders, along with their SSA.

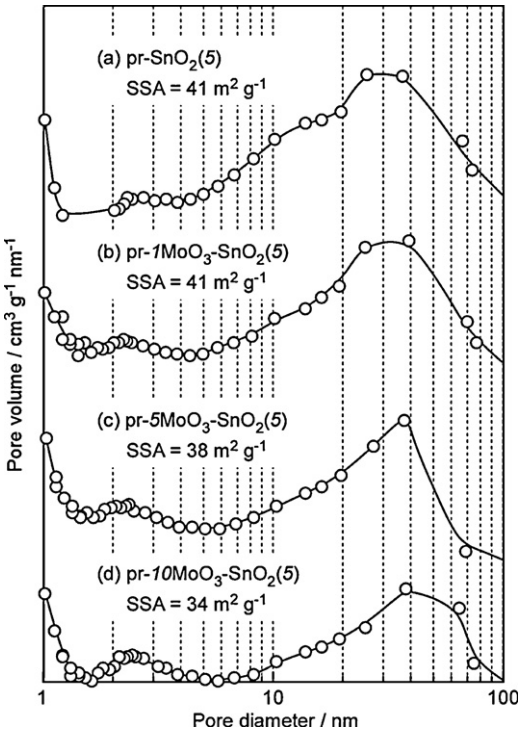

Fig. 5. Pore size distributions of pr–$SnO_2(5)$ and pr-$m$$MoO_3$–$SnO_2(5)$ powders, along with their SSA.

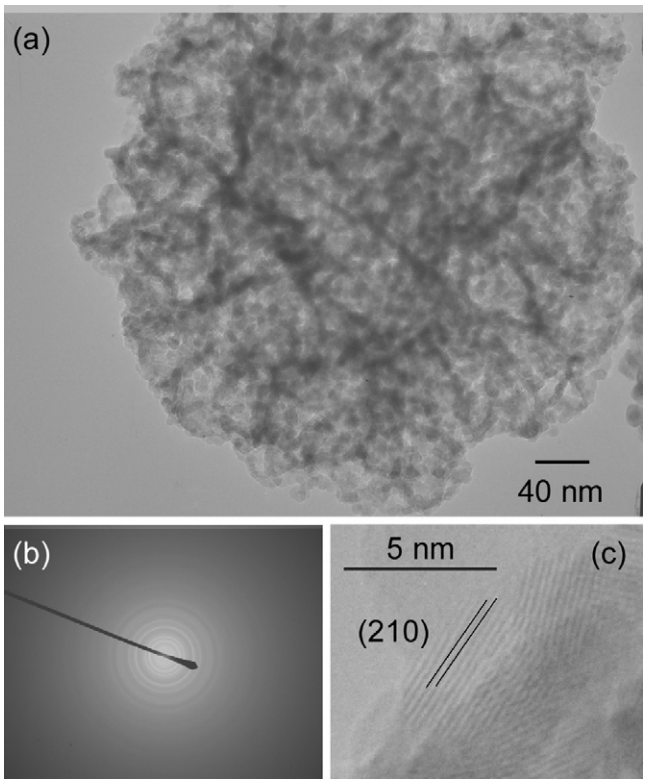

Fig. 6. (a) TEM image, (b) SAED pattern and (c) high-resolution transmission electron micrograph of pr–SnO_2(*5*).

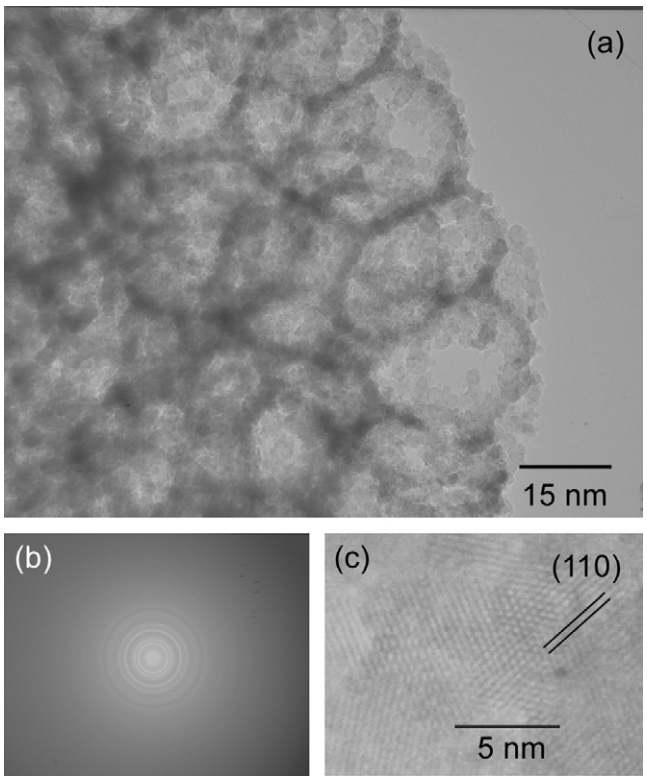

Fig. 7. (a) TEM image, (b) SAED pattern and (c) high-resolution transmission electron micrograph of pr-*10*MoO_3–SnO_2(*3*).

MoO_3 in pr-*m*MoO_3–SnO_2(*5*). Also, it showed that the amount of mesopores of ca. 30 nm in diameter decreased with an increase in the amount of MoO_3 with a slight increase in nanopores of ca. 2–3 nm in diameter. These results emphasize that nanopores of less than about 4 nm reflect the spaces formed among crystallites, while mesopores of about 30 nm seem to correspond to the spaces formed among crystallite agglomerates [14]. Considering the amount of addition of PMMA microspheres and the morphology of samples, it seems that all the molybdenum-components should be well-dissolved in $SnCl_4$ solutions. During the firing at elevated temperatures, OH^- and NH_4^+ removed as H_2O and NH_3, and MoO_3-doped SnO_2 was formed. Because, Mo^{6+} ions with an atomic radius of 0.42 Å can easily occupy the tin lattice sites (atomic radius of Sn^{4+} = 0.68 Å). But addition of 5 g PMMA microspheres may accelerate segregation of MoO_3 from the SnO_2 lattice. So, MoO_3 may be separately formed. The proposed mechanism was confirmed by EDX, SAED and TEM observations of pr-*10*MoO_3–SnO_2(*3*), pr-*10*MoO_3–SnO_2(*5*) and pr–SnO_2(*5*). Thus, the introduction of MoO_3 in the lattice of SnO_2 resulted in a decrease of the size of SnO_2 nanoparticles and an increase of the surface area.

Figs. 6–8 show TEM images of pr–SnO_2(*5*), pr-*10*MoO_3–SnO_2(*3*) and pr-*10*MoO_3–SnO_2(*5*), respectively, together with their SAED patterns. These figures indicated that the oxide walls consisted of very fine particles. The size of nanoparticles of pr-*10*MoO_3–SnO_2(*3*) is smaller than those of other two samples, and the spaces among their crystallites was in good agreement with the size of nanopores of the pore size distribution as shown in Figs. 4 and 5. Interestingly, large particles (sizes above 25 nm) cohabited among the small nanoparticles of pr-*10*MoO_3–SnO_2(*5*) (see Fig. 8a). The EDX results showed that they were related to pure MoO_3 phase, while the data is not shown here. This is perfectly in agreement with the BET analytical results. Namely, it indicates that the addition of large amount of PMMA microspheres (5 g) can accelerate segregation of

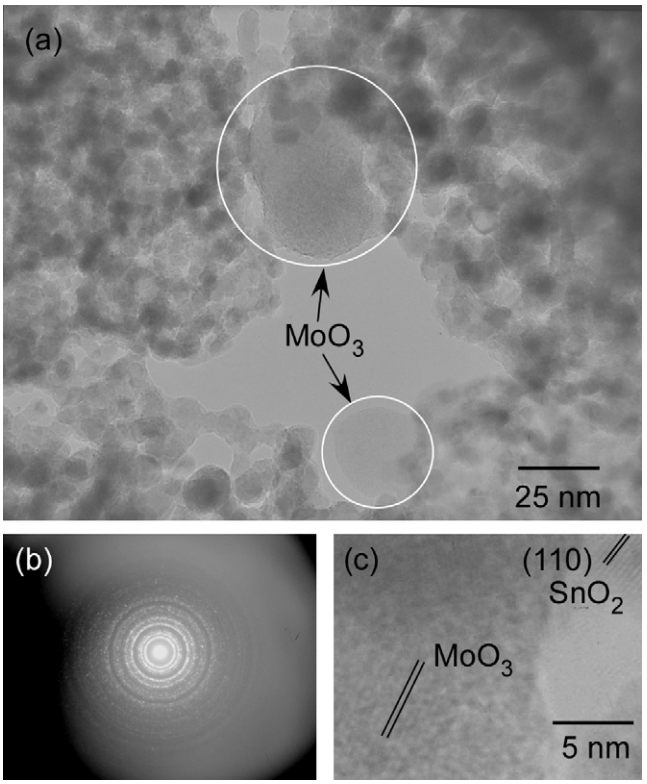

Fig. 8. (a) TEM image, (b) SAED pattern and (c) high-resolution transmission electron micrograph of pr-*10*MoO_3–SnO_2(*5*).

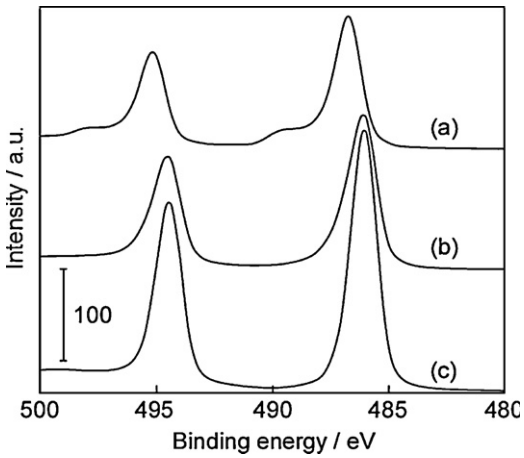

Fig. 9. XPS spectra of Sn3*d* for pr-*10*MoO_3–SnO_2(*n*): (a) *n* = 3, (b) *n* = 5, and (c) pr–SnO_2(*5*).

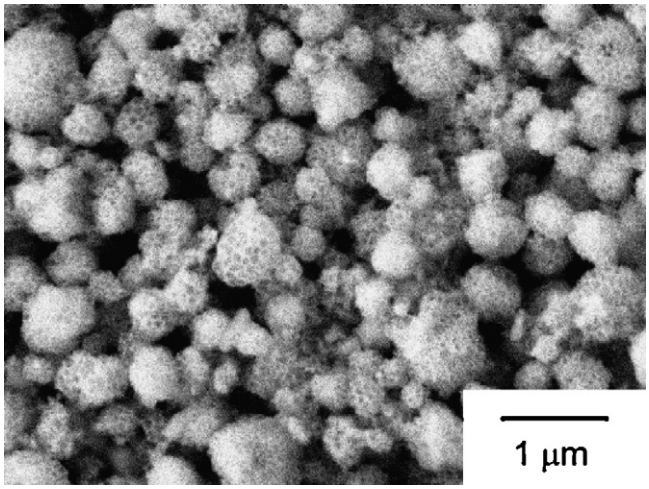

Fig. 11. SEM image of a pr-5MoO_3–SnO_2(*5*) thick film.

MoO_3 from the SnO_2 lattice and produces pure MoO_3 agglomerates.

SAED patterns of these three samples (Figs. 6(b), 7(b) and 8(b)) confirmed the well crystallization structure of their SnO_2 nanoparticles. The selected area exhibited distinctly three diffraction rings, which corresponded to the (1 1 0), (1 0 1) and (2 1 1) planes of the tetragonal-phase SnO_2 with rutile structure, respectively. With a careful observation of SAED pattern in Fig. 8(b), many bright spots could be indexed as a MoO_3 phase of large particles (above 25 nm), while faint rings were indexed as a cassiterite SnO_2 phase of small nanoparticles (6–10 nm).

On the other hand, the prepared products were polycrystalline as illustrated by high-resolution (HR) TEM observations (Figs. 6(c), 7(c) and 8(c)) consist of very fine particles. The spacing of the lattice fringes for pr-*10*MoO_3–SnO_2(*n*) (*n* = 3, and 5) and pr–SnO_2(*5*) was found to be 3.35 and 2.21 Å, respectively and these planes are best indexed as (1 1 0) and (2 1 0) of rutile SnO_2, respectively. Also, as shown in Fig. 8(c), the HRTEM image of MoO_3 particles revealed the clear lattice fringes illustrate the high crystallization of these particles. Therefore, MoO_3 phase which is stable up to 400 °C [15] existed in the pr-*10*MoO_3–SnO_2(*5*) even after firing at 1100 °C.

Figs. 9 and 10 show XPS spectra of Sn3*d* and Mo3*d* of pr–SnO_2(*5*) and pr-*10*MoO_3–SnO_2(*n*) (*n* = 3 and 5). The pr–SnO_2(*5*) exhibited two Sn3*d* peaks ($3d_{5/2}$ at 486.6 eV and $3d_{3/2}$ at 494.8 eV) and single peak of O1*s* at 530.4 eV (not shown here), which corresponded to the values of the lattice tin and lattice oxygen of general SnO_2, respectively [16]. The XPS spectra of Sn3*d* of pr-*10*MoO_3–SnO_2(*5*) showed slightly lower binding energy than those of pr–SnO_2(*5*). Interestingly, XPS spectra of Sn3*d* of pr-*10*MoO_3–SnO_2(*3*) showed relatively higher binding energy. These shifts may be explained by the presence of many Mo cations in SnO_2 lattices, creating an oxygen-rich surface layer on this sample [17]. On the other hand, the pattern observed for MoO_3 was due to the spin orbit splitting of Mo3*d* levels giving rise to $Mo3d_{5/2}$ and $Mo3d_{3/2}$ levels with an energy separation of 3.2 eV [18]. Binding energy of $Mo3d_{3/2}$ and $Mo3d_{5/2}$ levels for pr-*10*MoO_3–SnO_2(*3*) were observed at 233.3 eV and 236.5 eV, respectively. The values were close to the reported literatures [19] and confirmed that Mo was present mainly in 6+ oxidation state. However, XPS spectra of $Mo3d_{5/2}$ and $Mo3d_{3/2}$ of pr-*10*MoO_3–SnO_2(*5*) were 232 and 235.2 eV, respectively. Comparison of these values with standard ones reported in a literature [19] showed that they may correspond to Mo^{5+} ions.

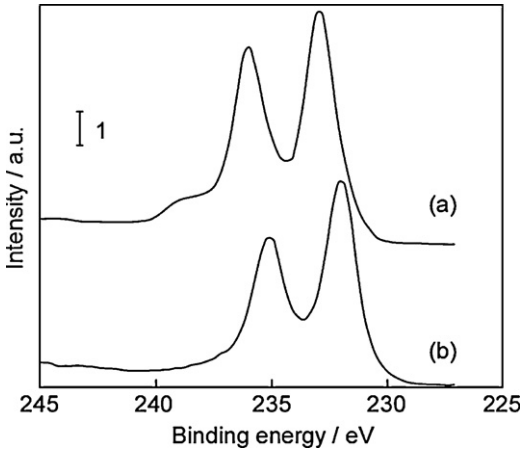

Fig. 10. XPS spectra of Mo3*d* for pr-*10*MoO_3–SnO_2(*n*): (a) *n* = 3 and (b) *n* = 5.

3.2. Gas-sensing properties of pr–SnO_2(*n*) and pr-*m*MoO_3–SnO_2(*n*) sensors

Fig. 11 shows a SEM image of surface of a pr-*5*MoO_3–SnO_2(*5*) sensor. The morphology is well-developed porous structure with clear boundaries among submicron-size porous SnO_2 particles, which were hardly destroyed during the fabrication process of the thick film. The morphology of other sensors was also similar to this sensor.

Figs. 12 and 13 show temperature dependence of response to 5 ppm NO_2 in air of all samples. Almost all samples showed the

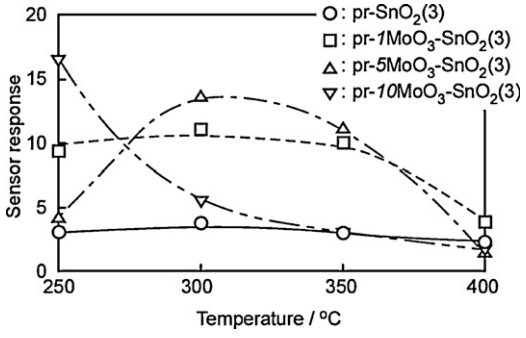

Fig. 12. Temperature dependence of response of pr–SnO_2(*3*) and pr-*m*MoO_3–SnO_2(3) (*m* = 1, 5 and 10) thick films to 5 ppm NO_2.

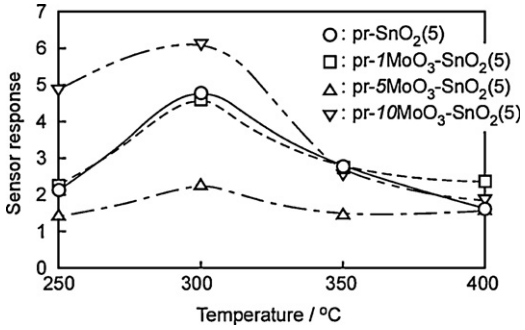

Fig. 13. Temperature dependence of response of pr–$SnO_2(5)$ and pr-$m$$MoO_3$–$SnO_2(5)$ (m = 1, 5 and 10) thick films to 5 ppm NO_2.

largest NO_2 response at 300 °C, except for pr-*10*MoO_3–$SnO_2(3)$. The excellent NO_2-response behavior of pr-$m$$MoO_3$–$SnO_2(n)$ can be understood from the following equation using Kröger–Vink notation:

$$MoO_3 \rightarrow Mo_{Sn}^{\bullet\bullet} + 2O_O^{x} + 1/2O_2 + 2e' \quad (1)$$

Therefore, according to Eq. (1), the increase in the adsorbed amount of NO_2 (negatively charged chemisorptions) is due to the increased concentration of electrons. It seems that an increase in the amount of Mo content leads to a significant increase of electrons and surface area and consequently an increase in sensor response. Therefore, the higher response at lower operating temperature of pr-*10*MoO_3–$SnO_2(3)$ sensor can be explained on the basis of high surface area and acidic nature of film. In addition, pr-*10*MoO_3–$SnO_2(5)$ film is more sensitive to NO_2 gas in comparison to other pr-$m$$MoO_3$–$SnO_2(5)$. Since the SSA of pr-*10*MoO_3–$SnO_2(5)$ is smaller than those of other pr-$m$$MoO_3$–$SnO_2(5)$, the higher response of pr-*10*MoO_3–$SnO_2(5)$ can be related to the amount of Mo species. Also, pr-$m$$MoO_3$–$SnO_2(3)$ films show relatively higher response than pr-$m$$MoO_3$–$SnO_2(5)$ films, probably because of larger surface area compared with that of pr-$m$$MoO_3$–$SnO_2(5)$ powders.

Fig. 14 shows response transients of pr–$SnO_2(3)$ and pr-$m$$MoO_3$–$SnO_2(3)$ samples at 350 °C. The recovery speed was slower with increasing the amount of MoO_3, probably due to slow desorption of NO_2^- and NO_3^- species which strongly bonded with molybdenum species on the surface. In addition, the resistance in air of all sensors was terribly high, probably due to the small grain size as well as a little number of boundaries among their submicron-size porous particles.

Figs. 15 and 16 show temperature dependence of responses to 100 ppm C_2H_5OH, 1000 ppm H_2 and 5 ppm NO_2 of pr-*10*MoO_3–$SnO_2(n)$ and pr–$SnO_2(n)$ sensors, respectively. The

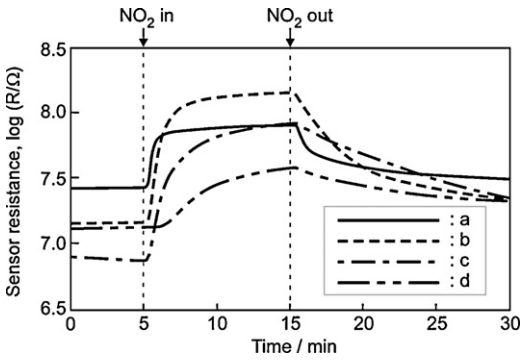

Fig. 14. Response transients of thick films of (a) pr–$SnO_2(3)$, (b–d) pr-$m$$MoO_3$–$SnO_2(3)$ powders (m = 1, 5 and 10), respectively.

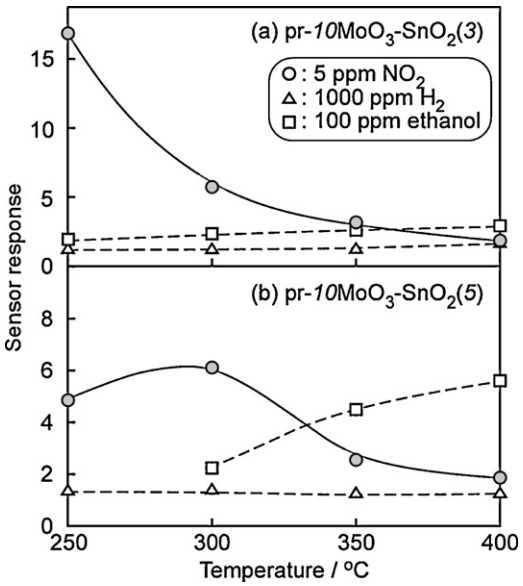

Fig. 15. Temperature dependence of response of pr-*10*MoO_3–$SnO_2(3)$ and pr-*10*MoO_3–$SnO_2(5)$ sensors.

addition of MoO_3 improved the sensor response and selectivity to NO_2 gas. Among them, pr-*10*MoO_3–$SnO_2(3)$ sensor showed large response to NO_2 and excellent selectivity to NO_2 at a low operating temperature of 250 °C, as shown in Fig. 15(a). On the other hand, Fig. 15(b) showed that pr-*10*MoO_3–$SnO_2(5)$ sensor showed large response to ethanol at higher temperature (400 °C) and large response to NO_2 gas at lower temperatures (300 °C).

On the other hand, pr–$SnO_2(n)$ sensors showed extremely large response to ethanol in comparison to other gases, as shown in Fig. 16. It shows that the presence of many acidic centers on the surface of thick films can reduce the sensor response to ethanol, because the ethanol conversion takes place with dehydration rout [20]. It seems that the presence of molybdenum species at the SnO_2 nano- and meso-porous structures changes their acidity performance which varies its reactivity versus certain gas species.

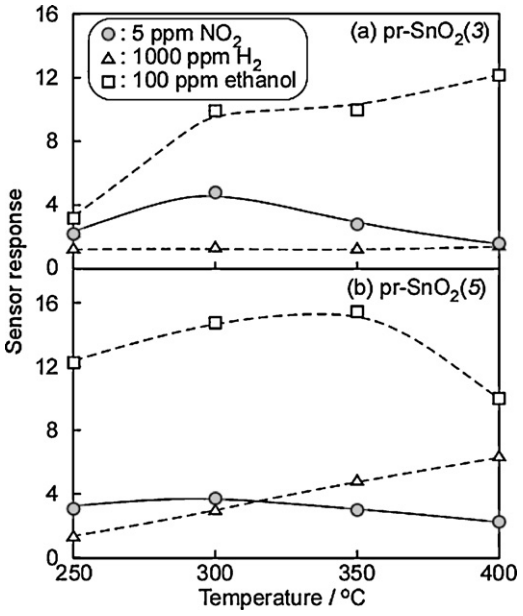

Fig. 16. Temperature dependence of response of pr–$SnO_2(3)$ and pr–$SnO_2(5)$ sensors.

4. Conclusion

pr–$SnO_2(n)$ and pr-$m$$MoO_3$–$SnO_2(n)$ powders with well-developed nano- and meso-porous structures have been synthesized by an ultrasonic spray-pyrolysis method. The results revealed that the use of PMMA microspheres as a template and the doping of MoO_3 affected on the structural, morphological and sensing properties of SnO_2 powders. The nano- and meso-porous SnO_2 powders were obtained by adding 3 and 5 g of PMMA microspheres in the precursor solution, respectively. Also, the addition of 5 g PMMA microspheres accelerated segregation of MoO_3 from the SnO_2 lattice. Namely, MoO_3 particles was separately formed among SnO_2 crystallites of pr-$m$$MoO_3$–$SnO_2(5)$ and then the surface area decreased. This phenomenon was confirmed by BET, TEM and EDX. On the other hand, the MoO_3-doping to pr–$SnO_2(n)$ improved the sensor response and selectivity towards NO_2 gas. This sensing behavior was well-correlated with the increase in acidity of the surface of the SnO_2 caused by the presence of molybdenum species in the SnO_2 nano- and meso-porous structures.

Acknowledgment

One of the authors (A. Anaraki Firooz) would like to acknowledge the sabatical leave awarded by the Ministry of Science and Technology of the Islamic Republic of Iran.

References

[1] A.A. Firooz, A.R. Mahjoub, A.A. Khodadadi, Effects of flower-like, sheet-like and granular SnO_2 nanostructures prepared by solid-state reactions on CO sensing, Mater. Chem. Phys. 115 (2009) 196–199.
[2] A.A. Firooz, A.R. Mahjoub, A.A. Khodadadi, Highly sensitive CO and ethanol nanoflower-like SnO_2 sensor among various morphologies obtained by using single and mixed ionic surfactant templates, Sens. Actuators B: Chem. 141 (2009) 89–96.
[3] A.A. Firooz, A.R. Mahjoub, A.A. Khodadadi, Preparation of SnO_2 nanoparticles and nanorods by using a hydrothermal method at low temperature, Mater. Lett. 62 (2008) 1789–1792.
[4] Z. Wen, G. Wang, W. Lu, Q. Wang, Q. Zhang, J. Li, Enhanced photocatalytic properties of mesoporous SnO_2 induced by low concentration ZnO doping, Cryst. Growth Des. 7 (2007) 1722–1725.
[5] Y.-H. Choi, M. Yang, S.-H. Hong, H_2 sensing characteristics of highly textured Pd-doped SnO_2 thin films, Sens. Actuators B: Chem. 134 (2008) 117–121.
[6] J.H. Pan, S.Y. Chai, C. Lee, S.-E. Park, W.I. Lee, Controlled formation of highly crystallized cubic and hexagonal mesoporous SnO_2 thin films, J. Phys. Chem. C 111 (2007) 5582–5587.
[7] J.Q. Sun, J.S. Wang, X.C. Wu, G.S. Zhang, J.Y. Wei, S.Q. Zhang, H. Li, D.R. Chen, Novel method for high-yield synthesis of rutile SnO_2 nanorods by oriented aggregation, Cryst. Growth Des. 6 (2006) 1584–1587.
[8] T. Hyodo, K. Sasahara, Y. Shimizu, M. Egashira, Preparation of macroporous SnO_2 films using PMMA microspheres and their sensing properties to NO_x and H_2, Sens. Actuators B: Chem. 106 (2005) 580–590.
[9] Z.A. Ansari, S.G. Ansari, T. Ko, J.-H. Oh, Effect of MoO_3 doping and grain size on SnO_2-enhancement of sensitivity and selectivity for CO and H_2 gas sensing, Sens. Actuators B: Chem. 87 (2002) 105–114.
[10] X. Jiaqiang, W. Ding, Q. Lipeng, Y. Weijun, P. Qingyi, SnO_2 nanorods and hollow spheres: controlled synthesis and gas sensing properties, Sens. Actuators B: Chem. 137 (2009) 490–495.
[11] J. Kaur, V.D. Vankar, M.C. Bhatnagar, Effect of MoO_3 addition on the NO_2 sensing properties of SnO_2 thin films, Sens. Actuators B: Chem. 133 (2008) 650–655.
[12] E. Zampiceni, E. Bontempi, G. Sberveglieri, L.E. Depero, Mo influence on SnO_2 thin films properties, Thin Solid Films 418 (2002) 16–20.
[13] J. Arbiol, J.R. Morante, P. Bouvier, T. Pagnier, E.A. Makeeva, M.N. Rumyantseva, A.M. Gaskov, SnO_2/MoO_3-nanostructure and alcohol detection, Sens. Actuators B: Chem. 118 (2006) 156–162.
[14] K. Hieda, T. Hyodo, Y. Shimizu, M. Egashira, Preparation of porous tin dioxide powder by ultrasonic spray pyrolysis and their application to sensor materials, Sens. Actuators B: Chem. 133 (2008) 144–150.
[15] F. Harb, B. Gerand, G. Nowogrocki, M. Figlarz, Structural filiation between a new molybdenum oxide hydrate ($MoO_3{\cdot}(1/3)H_2O$) and a new monoclinic form of MoO_3 obtained by dehydration, Solid State Ionics 32–33 (I) (1989) 84–90.
[16] S.G. Ansari, M.A. Dar, Y.-S. Kim, G.-S. Kim, H.-K. Seo, G. Khang, H.-S. Shin, Effect of growth temperature on the morphology and bonded states of SnO_2 nanobaskets, Appl. Surf. Sci. 253 (2007) 4668–4672.
[17] B. Mirkelamoglu, G. Karakas, The role of alkali-metal promotion on CO oxidation over PdO/SnO_2 catalysts, Appl. Catal. A: Gen. 299 (2006) 84–94.
[18] C.D. Wagner, W.M. Riggs, L.E. Davis, J.F. Moulder, G.E. Muilenberg, Handbook of X-ray Photoelectron Spectroscopy, Physical Electronics Division, Perkin-Elmer, Eden Prairie, Minnesota, 1979.
[19] Y. Zhang, J. Yuan, Y. Cao, L. Song, X. Hu, Photochromic behavior of Li-stabilized MoO_3 sol–gels, J. Non-Cryst. Solids 354 (2008) 1276–1280.
[20] N. Yamazoe, G. Sakai, K. Shimanoe, Oxide semiconductor gas sensors, Catalysis Surveys from Asia 7 (2003) 63–75.

Biographies

A. Anaraki Firooz received MSc degree in inorganic chemistry from Tarbiat Modares University in 2005. She is a PhD student at the Department of Chemistry under the supervisions of Prof. A.R. Mahjoub and Prof. A.A. Khodadadi. Her research project focuses on "The effect of morphology and additives on sensing and catalytic functions of SnO_2 nanostructures". She is now a visiting researcher in Nagasaki University.

T. Hyodo received his B. Eng. degree in applied chemistry and M. Eng. degree in materials science and technology in 1992 and 1994, respectively, and Dr. Eng. degree in 1997 from Kyushu University. He has been an assistant professor at Nagasaki University since 2007. His research interests are the developments of electrochemical devices such as chemical sensors and lithium batteries, and mesoporous and macroporous materials.

A.R. Mahjoub received his MS in organic chemistry in 1988 and his PhD in inorganic chemistry in 1993 from University of Berlin, Germany. His research activity covers many aspects of the synthesis, characterization and chemical–physics of metal oxides and nanooxides with particular emphasis to catalytic and photo degradation properties.

A. Khodadadi received his MS in chemical engineering from the University of Tehran in 1986 and his PhD in catalysis and reaction engineering from University of Waterloo, Canada, in 1994. His research interests include catalysis, reaction engineering, and nanostructured materials as applied to nanoparticles, carbon nanotubes, plasma-catalytic conversion of natural gas to liquids and chemicals, metal oxide semiconductor gas sensors, air pollution control using catalytic converters and oxygen sensors using solid electrolytes.

Y. Shimizu received his BE degree in applied chemistry in 1980 and Dr. Eng. degree in 1987 from Kyushu University. He has been a professor at Nagasaki University since 2005. His current research concentrates on development of odor sensors and design of intelligent sensors by controlling gas diffusivity and reactivity.